

# *Spatiotemporal Monitoring of Air Quality ( $PM_{10}$ , $SO_2$ , & $NO_2$ ) in Semarang City Using Landsat Satellite Imagery*

Abdi Sukmono, Diah Septiyana, Muhammad Adnan Yusuf, Arwan Putra Wijaya

Department of Geodetic Engineering, Faculty of Engineering, Diponegoro University, Semarang, Indonesia

Email : sukmono35@gmail.com or abdisukmono@lecturer.undip.ac.id



**Abstract** — Air quality is a critical environmental parameter, heavily influenced by local human activities. Intense human and industrial activities in large urban areas significantly degrade air quality, contributing to climate change and adversely affecting public health. Therefore, monitoring air quality in major cities is vital for ensuring environmental sustainability. This study aims to monitor air quality in the Mijen District of Semarang City, Indonesia, utilizing a spatiotemporal approach. The air quality parameters assessed in this study included  $PM_{10}$ ,  $SO_2$ , and  $NO_2$ , which were derived from Landsat 8 and Landsat 9 satellite imagery data. The analysis employed a spatiotemporal method based on the Global Moran's I Index and the Local Indicator of Spatial Autocorrelation (LISA) to elucidate spatial distribution patterns and temporal trends. The results indicated that the air quality in the Mijen District of Semarang City—based on the parameters  $PM_{10}$ ,  $SO_2$ , and  $NO_2$ —largely met the Air Quality Standard Index thresholds. However, several locations exhibited significantly high pollution levels that formed clusters and showed temporal consistency. These high pollution levels were observed in specific land use areas, such as industrial zones, residential areas, and landfill sites. The lowest  $PM_{10}$  levels were recorded in April 2021 and June 2021, ranging from 0 to  $19 \mu\text{g}/\text{m}^3$ , with a spread over an area of  $57 \text{ km}^2$ . The highest  $SO_2$  concentration was observed in August 2021, exceeding 300 ppm. Additionally, the highest  $NO_2$  distribution was also recorded in August 2021, with values ranging from 179 to  $180 \mu\text{g}/\text{m}^3$ .

**Keywords**—Spatial Autocorrelation, Landsat Imagery, Global Moran's I Index, Air Pollution, Spatiotemporal Analysis.

## I. INTRODUCTION

Air pollution is a critical issue for many major cities worldwide [1,2]. It is especially prevalent in densely populated urban areas [3]. High levels of traffic and industrial activities in these cities contribute to declining air quality [4]. According to WHO data, over 80% of urban residents are exposed to air that is unhealthy or below WHO standards [5]. This significantly impacts public health, posing a challenge that must be addressed by cities globally as urbanization continues [6].

Air pollution can be measured by several key parameters, including sulfur dioxide, nitrogen dioxide, and carbon dioxide [7]. These pollutants are generated by various combustion processes such as industrial activities, motor vehicle emissions, and land burning [8]. Exposure to these pollutants beyond acceptable limits can cause severe health issues [9]. Furthermore, airborne particles like particulate matter ( $PM_{2.5}$  and  $PM_{10}$ ) are also critical indicators of air quality. These particles can impair the human respiratory system and lead to significant health problems [10].

The monitoring of air quality in large urban centers is paramount for safeguarding human health [11]. It stands as a fundamental measure in mitigating potential environmental pollution and demands continuous implementation. Real-time monitoring of air quality data functions as an early warning mechanism for air pollution [12]. Technology plays a pivotal role in acquiring precise air quality metrics for each geographical area. Virtually all major cities have established monitoring systems utilizing data from air quality monitoring stations. However, achieving granularity in data per locale necessitates a substantial

network of stations. Technological advancements are indispensable in addressing this challenge and acquiring spatially accurate air quality data.

Current air quality monitoring can also leverage satellite technology [13]. This innovative approach facilitates the acquisition of air quality parameters through satellite sensors. For instance, as illustrated by [14], the utilization of xx satellite imagery enables the retrieval of SO<sub>2</sub> and NO<sub>2</sub> parameters in the atmosphere. Similarly, the extraction of PM<sub>10</sub> air quality parameters can be achieved using Landsat satellite imagery, as exemplified by [15]. The data extracted from satellite imagery holds the capability to visualize spatial air quality information, significantly enhancing our comprehension of air quality distribution within a given region. Consequently, spatial analysis methodologies can be employed to implement mitigation strategies against air pollution.

Semarang City stands as one of Indonesia's burgeoning metropolitan hubs. Its continuous expansion has precipitated a decline in Green Open Space (GOS), potentially impacting air quality [16]. Among the swiftly evolving districts within Semarang City is the Mijen District [17]. Marked by substantial development, this area is integral to the city's urbanization blueprint. Notably, land use transformations here are significant, witnessing the conversion of various zones into residential, commercial, service, and industrial sectors. Such transitions are suspected to exert an influence on air quality. Hence, this study endeavors to conduct spatiotemporal air quality monitoring in the Mijen District of Semarang City, utilizing Landsat image data. Anticipated outcomes include a comprehensive portrayal of air quality conditions in Semarang City, serving as a foundational resource for mitigation strategies.

## II. MATERIALS AND METHODS

### 2.1. RESEARCH LOCATION AND DATA

This study was carried out in Semarang City, focusing on the Mijen District as a case study. This district is undergoing development within Semarang City. The land use in the Mijen district is diverse, encompassing residential, industrial, plantation, farming, trade and services, and public utilities.

Air quality data was derived from the processing of Landsat 8 and Landsat 9 images, with acquisition dates as outlined in Table 1.

Table 1. Landsat Data

Images	Acquisition Date
Landsat 8 Level-1	April 24, 2020
	May 10, 2020
	June 11, 2020
	April 27, 2021
	June 30, 2021
	August 17, 2021
Landsat 9 Level-1	April 22, 2022
	July 22, 2022

### 2.2. THE BASIC ALGORITHM FOR SATELLITE IMAGE PARAMETERS

The processing of air quality algorithms necessitates fundamental land surface temperature (LST) data extracted from Landsat 8. The mono window algorithm (MWA) is applied to ascertain the estimated land surface temperature (LST) values. This algorithm factors in surface emissivity and vegetation proportion (PV) during the LST estimation. Calculating the normalized difference vegetation index (NDVI) is imperative to derive the PV value, which is essential for obtaining the surface emissivity value.

1. Calculation of Normalized Difference Vegetation Index (NDVI)

The normalized difference vegetation index (NDVI) serves as an indicator of vegetation greenness or photosynthetic activity, representing one of the most prevalent vegetation indices. NDVI is computed as the ratio between the measured reflectance of the red band (R) and the near-infrared band (NIR). NDVI values range from -1 to +1 [18]. The NDVI calculation formula is as follows.

$$NDVI = \frac{(NIR-RED)}{(NIR+RED)} \dots\dots\dots (1)$$

Where:

NIR = Near-infrared radiation (band 5);

Red = Red radiation (band 4).

2. Calculation of Proportion of Vegetation (PV)

The estimation of PV values is based on previously acquired NDVI values, along with the NDVI<sub>s</sub> (representing soil or minimum) and NDVI<sub>v</sub> (representing vegetation or maximum) values derived from the NDVI data [19]. PV is calculated using the equation below.

$$PV = \left( \frac{NDVI-NDVI_{min}}{NDVI_{max}-NDVI_{min}} \right)^2 \dots\dots\dots (2)$$

Where:

NDVI<sub>min</sub> (Soil) = The NDVI value for soil (0.2);

NDVI<sub>max</sub> (Vegetation) = The NDVI value for vegetation (the highest NDVI value).

3. Calculation of Emissivity (E)

Emissivity gauges the inherent characteristics of the Earth’s surface and its capacity to convert heat energy into radiative energy [19]. The formula for emissivity calculation is as follows.

$$e = 0.004PV + 0.986 \dots\dots\dots (3)$$

Where:

*e* = Emissivity;

*PV* = Proportion of Vegetation.

4. Calculation of Brightness Temperature (BT)

Brightness temperature (BT) signifies the upward journey of electromagnetic radiation from the Earth’s atmosphere [20]. The BT equation is outlined as follows.

$$BT = \frac{K2}{\ln \left( \frac{K1}{L\lambda} + 1 \right)} - 273.15 \dots\dots\dots (4)$$

Where:

*Lλ* = Spectral radiance TOA

*K1* = Specific thermal conversion constant for the band;

*K2* = Specific thermal conversion constant for the band.

5. Calculation of Land Surface Temperature (LST)

Land surface temperature (LST) for bands 10 and 11 is determined using the equation below.

$$LST = \left( \frac{BT}{(1 + (\lambda \cdot \frac{BT}{c^2}) \cdot \ln(E))} \right) \dots\dots\dots (5)$$

Where:

*BT* = Brightness temperature (°C);

$\lambda$  = Emitted wavelength;

*E* = Surface emissivity;

$c^2$  = Derived from  $h \times \frac{c}{s} = 1.4388 \times 10^{-2} \text{ mk} = 14.388 \text{ mk}$  [where *h* denotes Planck’s constant ( $6.626 \times 10^{-34} \text{ Js}$ ); *s* denotes Boltzmann’s constant ( $1.38 \times 10^{-23} \text{ JK}$ ); *c* denotes the speed of light ( $2.998 \times 10^8 \text{ m/s}$ )].

**2.3. AIR QUALITY ALGORITHM**

Below is the algorithm utilized to determine the content and distribution of air pollutants.

1. Measurement of PM10

The algorithmic formula for PM10, as presented in [21], is a modification of the algorithm proposed by [22].

$$PM_{10} = (96 \times BR\rho) + (253 \times BG\rho) - (194 \times BB\rho) \dots\dots\dots (6)$$

Where: PM10 denotes aerosol particulates ( $\mu\text{g/m}^3$ ); *BR* $\rho$  represents the reflectance of the *BoA* red band; *BG* $\rho$  represents the reflectance of the *BoA* green band; *BB* $\rho$  represents the reflectance of the *BoA* blue band.

2. Measurement of SO2

The algorithm for SO2, detailed in [18], is expressed as follows.

$$SO_2 = 0.0117T^3 - 0.3282T^2 + 2.837T - 6.4733 \dots\dots\dots (7)$$

Where: SO2 indicates the concentration of sulfur dioxide in the air (ppm); *T* signifies the value of LST temperature.

3. Measurement of NO2

The NO2 calculation algorithm derived from Landsat satellite image processing, as outlined in [23], is as follows.

$$NO_2 = 163.88 + 0.3908 \times T \dots\dots\dots (8)$$

Where: NO2 represents the concentration of nitrogen dioxide gas ( $\mu\text{g/m}^3$ ); *T* denotes the value of LST temperature.

**2.4. SPATIOTEMPORAL PATTERN PROCESSING METHOD**

Spatial distribution patterns were analyzed using Global Moran’s *I* Index spatial autocorrelation, while distribution patterns were analyzed using the Local Indicator of Spatial Autocorrelation (LISA). The Global Moran’s *I* Index can determine the spatial autocorrelation patterns formed, which may take the form of dispersed, random, or clustered patterns. LISA identifies local autocorrelation in each area. Calculating Global Moran’s *I* Index requires the mean and variance values of the data, as well as understanding how each feature relates to its neighbors. Then, the difference between the value of each feature and the mean is compared with the difference between the values of its neighbors and the mean. If the differences are in the same direction (both positive or both negative), it indicates similar features. If the differences are in opposite directions (one positive and one negative), it indicates different features. The Global Moran’s *I* Index value is represented in Equation 9 below.

$$I = \frac{n}{\sum_{i=1}^n \sum_{j=1}^n w_{ij}} \frac{\sum_{i=1}^n \sum_{j=1}^n w_{ij} (x_i - \bar{x})(x_j - \bar{x})}{\sum_{i=1}^n (x_i - \bar{x})^2} \dots\dots\dots (9)$$

Where:

$x_i$  = data variable at location *i*

$x_j$  = data variable at location  $j$

$\bar{x}$  = mean of the data

$w$  = weight matrix

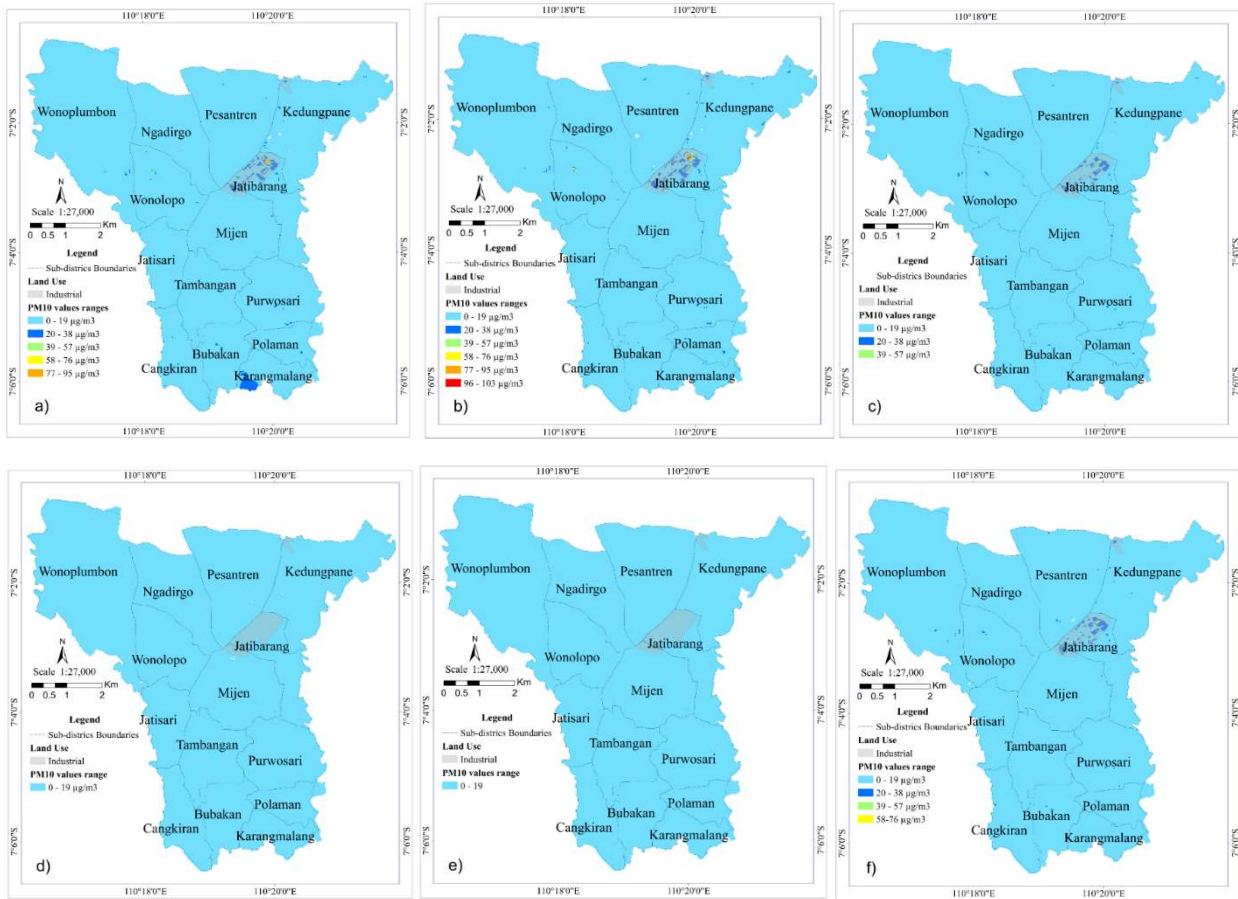
The Moran's  $I$  Index ranges from -1 to 1. A value of  $I > I_0$  indicates a tendency towards clustering patterns, while a value of  $I < I_0$  signifies dispersed patterns.  $I_0$  represents the expected value of  $I$ , and its formula can be found in Equation 10 below.

$$E(I) = I_0 = -\frac{1}{n-1} \dots \dots \dots (10)$$

### III. RESULTS AND DISCUSSION

#### A. ANALYSIS OF THE PM10 PARAMETER

Visually, it is apparent from Figure 1 that the PM10 distribution predominantly falls within the range of 0–19 µg/m³. The highest PM10 distribution values are observed in the Jatibarang and Mijen Subdistricts, both of which harbor industrial areas. The May 2020 image reveals the widest range of values, ranging from 96–103 µg/m³. Conversely, the images from April 2021 and June 2021 depict the lowest range of values, limited to the 0–19 µg/m³ range. The decline in PM10 distribution values in April 2021 can be attributed to the implementation of community activity restrictions coinciding with the 2021 Eid al-Fitr holiday. Conversely, the reduction in PM10 values in June 2021 was a result of the emergency enforcement of these activity restrictions.



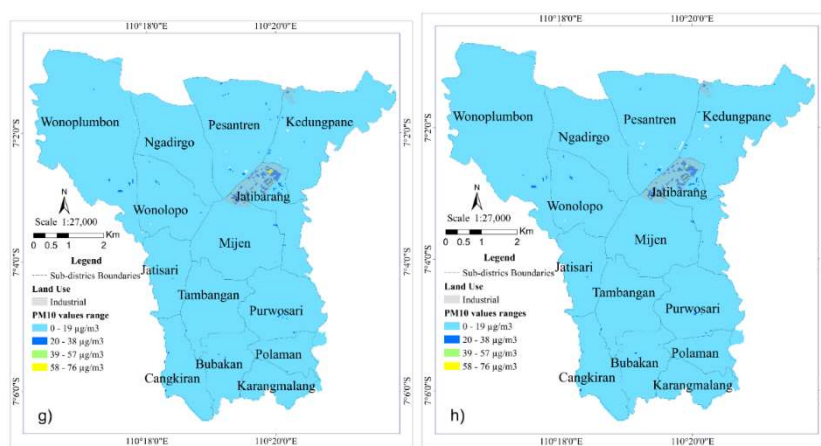


Figure 1. Distribution of PM<sub>10</sub> in (a) April 2020, (b) May 2020, (c) June 2020, (d) April 2021, (e) June 2021, (f) August 2021, (g) April 2022, and (h) July 2022

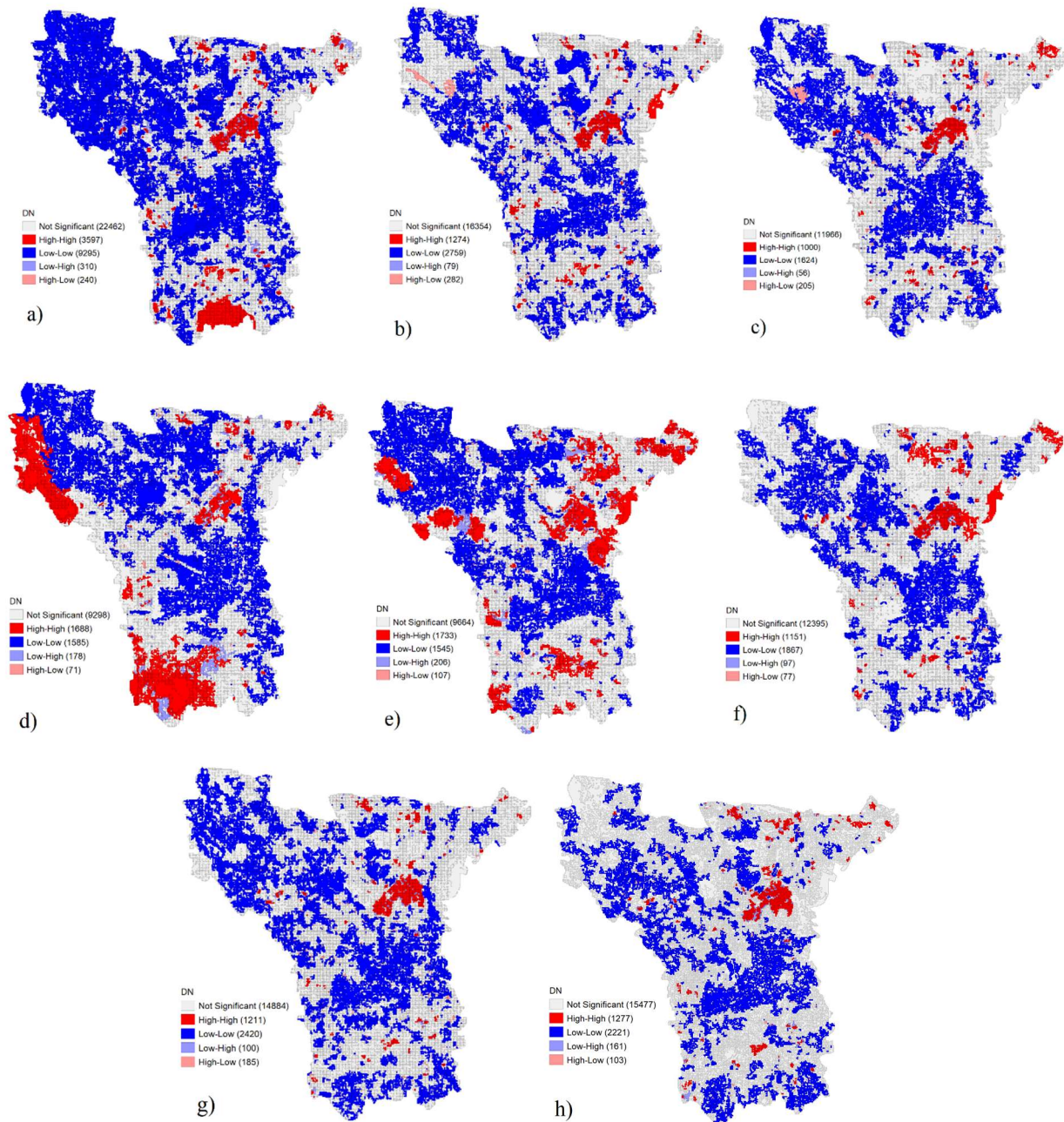
The patterns resulting from the Global Moran's *I* Index processing are presented in Table 2 below.

Table 2. Global Moran's *I* Index Results of PM<sub>10</sub>

Acquisition Date	<i>p</i> -value	z-score	Pattern
April 24, 2020	0.043787	2.016122	clustered
May 10, 2020	0.866075	-0.168647	random
June 11, 2020	0	469.587817	clustered
April 27, 2021	0	249.87480	clustered
June 30, 2021	0	161.133138	clustered
August 17, 2021	0	427.343256	clustered
April 22, 2022	0	509.017196	clustered
July 22, 2022	0	389.746739	clustered

From Table 2, it can be deduced that all image processing outcomes demonstrate clustered spatial patterns, except for May 2020, which exhibits a random pattern.

The distribution patterns of PM<sub>10</sub> are scrutinized using the Local Indicator of Spatial Autocorrelation (LISA) with a queen contiguity weight matrix.



**Figure 2.** LISA's PM<sub>10</sub> Distribution Patterns in (a) April 2020, (b) May 2020, (c) June 2020, (d) April 2021, (e) June 2021, (f) August 2021, (g) April 2022, and (h) July 2022

From the LISA autocorrelation findings, it can be inferred that industrial and landfill areas exhibit clustered patterns and are characterized by a High-High (H-H) spatial relationship, indicating elevated PM<sub>10</sub> levels in these areas and their vicinity. Conversely, other regions show Low-Low (L-L) relationships, denoted by blue color, and insignificant relationships, represented by gray color.

B. ANALYSIS OF THE SO<sub>2</sub> PARAMETER

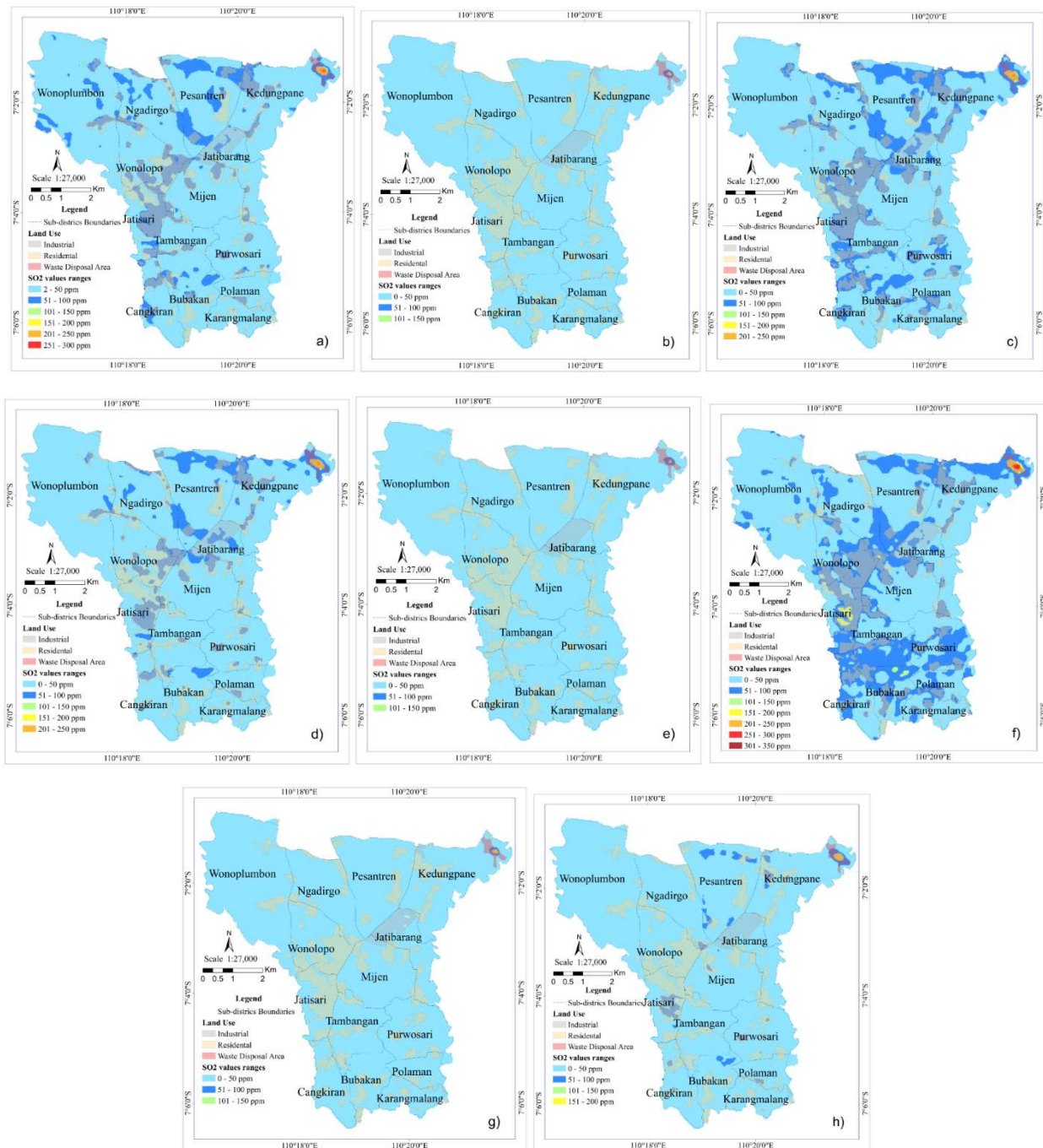


**Figure 3.** Distribution of SO<sub>2</sub> in (a) April 2020, (b) May 2020, (c) June 2020, (d) April 2021, (e) June 2021, (f) August 2021, (g) April 2022, and (h) July 2022

From Figure 3, it is evident that SO<sub>2</sub> distribution is predominantly in the range of 0–50 ppm, with the highest values observed in the Jatibarang Landfill Site in Kedungpane Subdistrict. SO<sub>2</sub> distribution in the range of 51–100 ppm is scattered in residential areas.

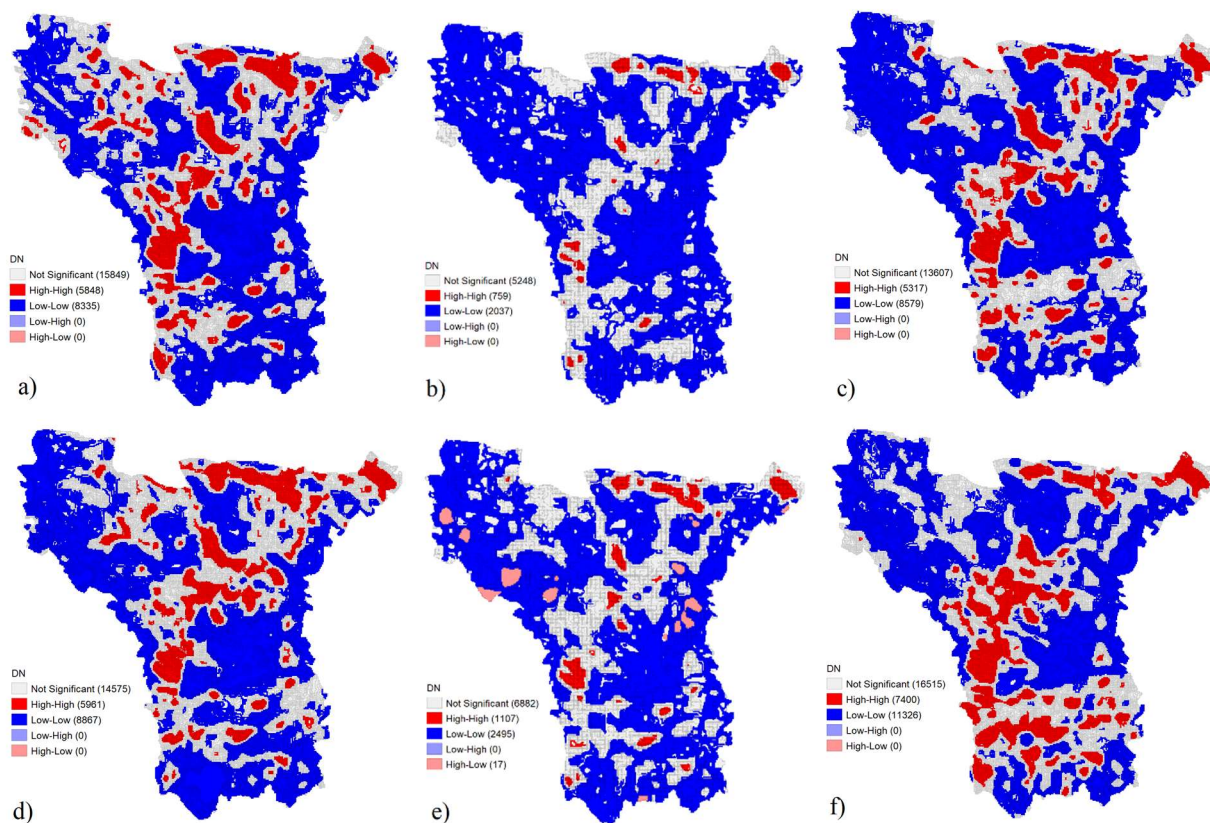
The spatial patterns resulting from Global Moran’s *I* Index processing are presented in Table 3 below.

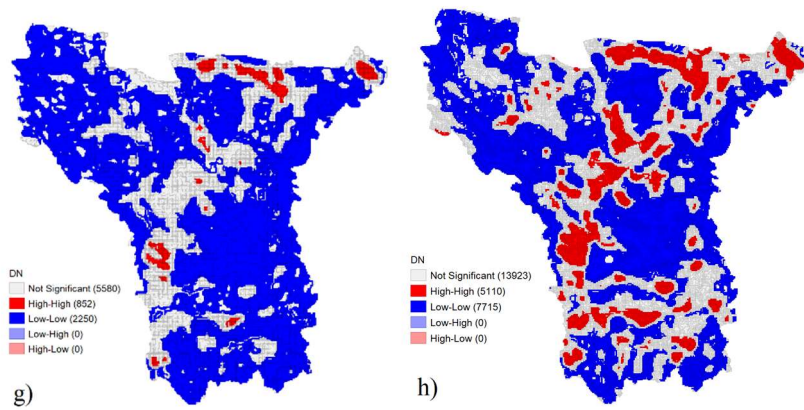
Table 3. Global Moran's *I* Index Results of SO<sub>2</sub>

Acquisition Date	<i>p</i> -value	<i>z</i> -score	Pattern
April 24, 2020	0	950.5935532	clustered
May 10, 2020	0	527.873419	clustered
June 11, 2020	0	887.269361	clustered
April 27, 2021	0	1036.994279	clustered
June 30, 2021	0	767.080606	clustered
August 17, 2021	0	1036.008230	clustered
April 22, 2022	0	557.835834	clustered
July 22, 2022	0	895.698008	clustered

Table 3 illustrates that all datasets demonstrate clustered spatial patterns. Across all datasets, the *p*-value is 0, with *z*-score values exceeding 1, indicating a clustered pattern.

The distribution patterns of SO<sub>2</sub> are further analyzed using the Local Indicator of Spatial Autocorrelation (LISA) with a queen contiguity weight matrix.

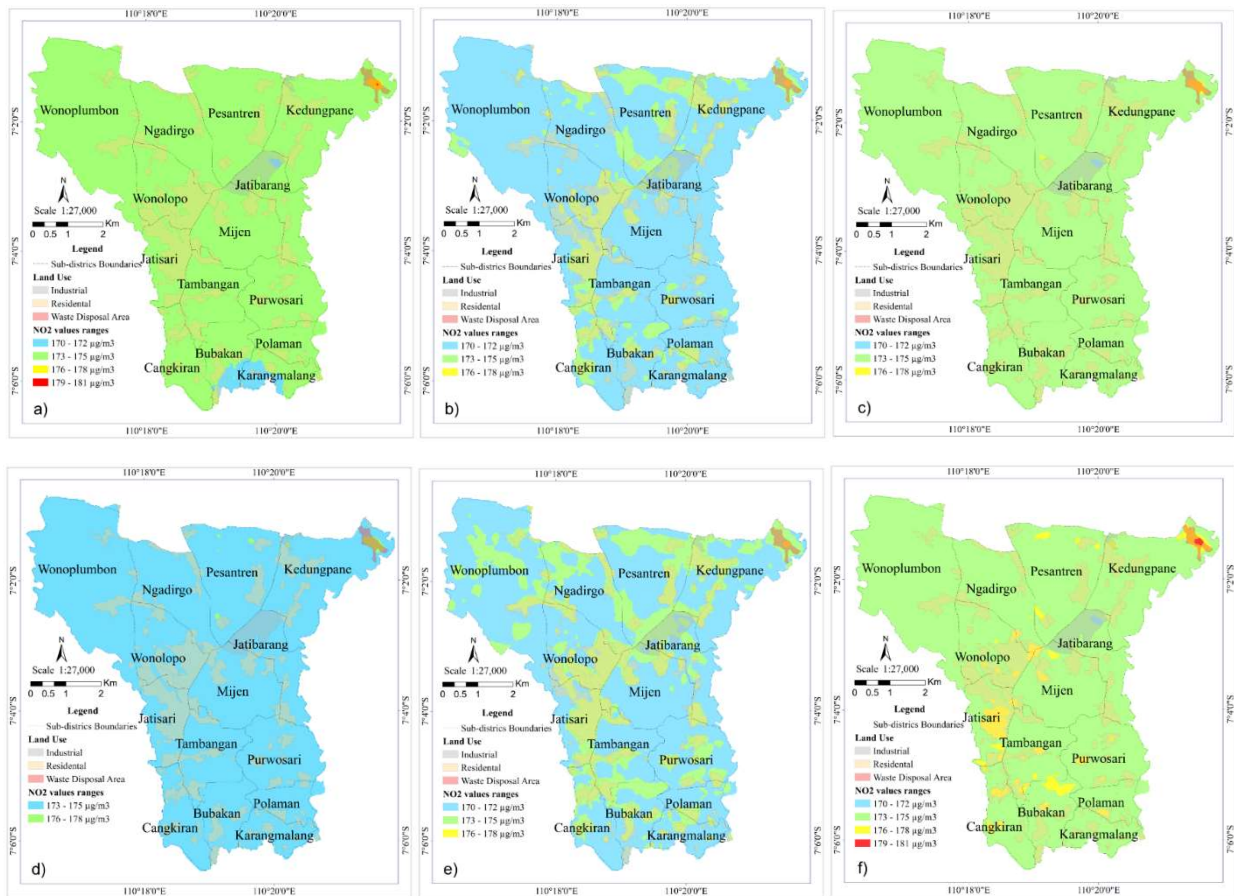




**Figure 4.** LISA’s SO<sub>2</sub> Distribution Patterns in (a) April 2020, (b) May 2020, (c) June 2020, (d) April 2021, (e) June 2021, (f) August 2021, (g) April 2022, and (h) July 2022

The LISA autocorrelation results suggest that landfill areas and several other regions demonstrate clustered patterns, characterized by a High-High (H-H) spatial relationship. This suggests elevated SO<sub>2</sub> levels in these areas and their vicinity. Conversely, other regions exhibit a Low-Low (L-L) spatial relationship, indicating lower SO<sub>2</sub> levels in these areas and their surroundings.

*C. ANALYSIS OF THE NO<sub>2</sub> PARAMETER*



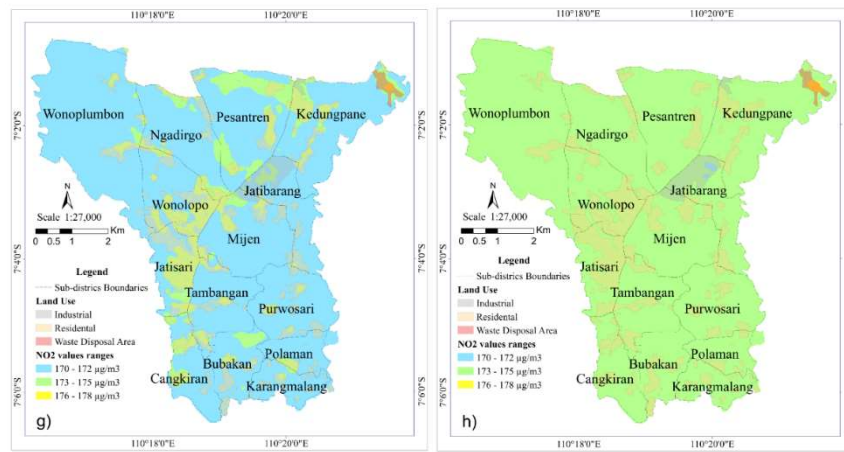


**Figure 5.** Distribution of NO<sub>2</sub> in (a) April 2020, (b) May 2020, (c) June 2020, (d) April 2021, (e) June 2021, (f) August 2021, (g) April 2022, and (h) July 2022

From the image data shown in Figure 5, variations in color and range are apparent. The blue color indicates NO<sub>2</sub> distribution in the range of 170–172 µg/m<sup>3</sup>, while the green color indicates NO<sub>2</sub> distribution in the range of 173–175 µg/m<sup>3</sup>. Based on the distribution, the highest NO<sub>2</sub> values are observed in the landfill area.

The patterns resulting from the Global Moran’s *I* Index processing are presented in Table 4 below.

**Table 4.** Global Moran’s *I* Index Results of NO<sub>2</sub>

Acquisition Date	<i>p</i> -value	z-score	Pattern
April 24, 2020	0	9.128566	clustered
May 10, 2020	0	6.720208	clustered
June 11, 2020	0	6.403769	clustered
April 27, 2021	0.000001	4.890143	clustered
June 30, 2021	0.155013	-1.422046	random
August 17, 2021	0	15.799382	clustered
April 22, 2022	0	5.401616	clustered
July 22, 2022	0.029464	2.177221	clustered

From this figure it is evident that all datasets exhibit clustered spatial patterns, except for June 2021, which shows a random pattern.

The distribution patterns of NO<sub>2</sub> are analyzed using the Local Indicator of Spatial Autocorrelation (LISA) with a queen contiguity weight matrix.

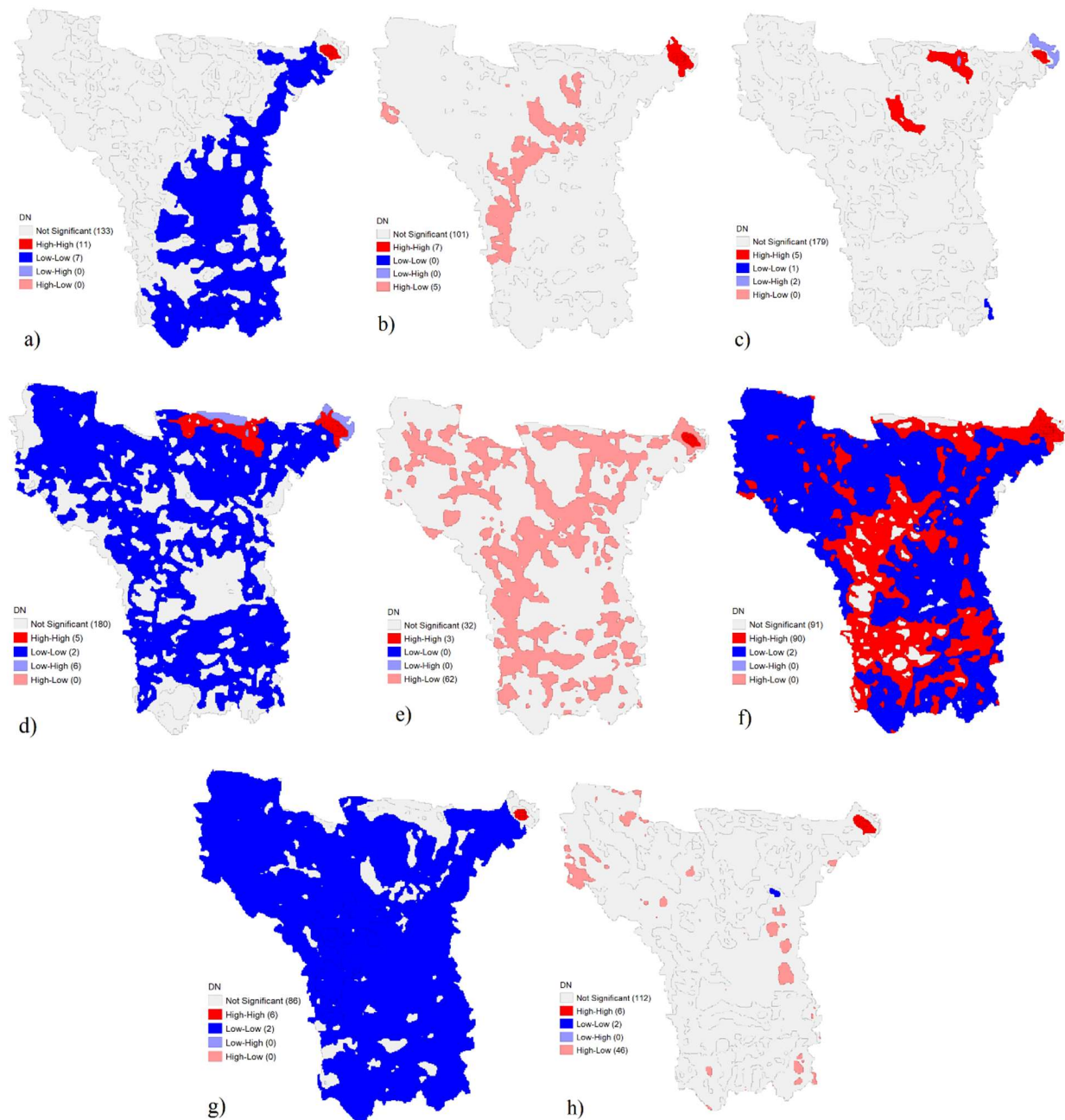


**Figure 6.** LISA's NO<sub>2</sub> Distribution Patterns in (a) April 2020, (b) May 2020, (c) June 2020, (d) April 2021, (e) June 2021, (f) August 2021, (g) April 2022, and (h) July 2022

From the spatial autocorrelation analysis using LISA, it can be inferred that the landfill areas exhibit a High-High (H-H) spatial relationship, suggesting that the NO<sub>2</sub> concentrations in these areas and their surroundings are high. Conversely, other areas display a clustered pattern and a Low-Low (L-L) spatial relationship, indicating lower NO<sub>2</sub> concentrations surrounded by areas with similarly low NO<sub>2</sub> levels. Moreover, in certain areas, there is a non-significant spatial relationship, signifying no substantial disparity in NO<sub>2</sub> concentrations between adjacent regions.

#### IV. CONCLUSIONS

Overall, the air quality in Semarang City from 2020 to 2022 remains generally satisfactory, meeting air quality standards. However, certain areas exhibit significant air pollution with a clustered pattern. All three air quality parameters (PM<sub>10</sub>, SO<sub>2</sub>, and NO<sub>2</sub>) display clustered distributions. The distribution of PM<sub>10</sub> shows a notable clustering, particularly with the highest values

detected in industrial zones. Similarly, the distribution of SO<sub>2</sub> demonstrates significant clustering, notably with elevated levels observed in the Jatibarang Landfill Site, alongside moderate levels in industrial and residential areas. Likewise, the distribution of NO<sub>2</sub> exhibits significant clustering, with the highest concentrations detected in the Jatibarang Landfill Site, and moderate concentrations observed in industrial and residential areas.

### REFERENCES

- [1] M.E. Marlier, A.S. Jina, P.L. Kinney. "Extreme Air Pollution in Global Megacities". *Curr Clim Change Rep* 2, 15–27 (2016). <https://doi.org/10.1007/s40641-016-0032-z>
- [2] A. Piracha, M. T. Chaudhary. "Urban Air Pollution, Urban Heat Island and Human Health: A Review of the Literature". *Sustainability* 2022, 14, 9234. <https://doi.org/10.3390/su14159234>
- [3] Rainald Borck, Philipp Schrauth. Population density and urban air quality. *Regional Science and Urban Economics*, Volume 86, 2021,103596 , <https://doi.org/10.1016/j.regsciurbeco.2020.103596> .
- [4] M. Maione, E. Mocca, K. Eisfeld. "Public perception of air pollution sources across Europe". *Ambio* 50, 1150–1158 (2021). <https://doi.org/10.1007/s13280-020-01450-5>
- [5] A. Piracha, M.T. Chaudhary. "Urban Air Pollution, Urban Heat Island and Human Health: A Review of the Literature". *Sustainability*. 2022; 14(15):9234. <https://doi.org/10.3390/su14159234>
- [6] C. Zhan, M. Xie, H. Lu. Impacts of urbanization on air quality and the related health risks in a city with complex terrain. *Atmospheric Chemistry and Physics*. Vol.23 No 1 (771-788). <https://doi.org/10.5194/acp-23-771-2023>
- [7] T. M. Chen, W. G. Kuschner, J. Gokhale, S. Shofer. "Outdoor Air Pollution: Nitrogen Dioxide, Sulfur Dioxide, and Carbon Monoxide Health Effects". *The American Journal of the Medical Sciences*. Volume 333, Issue 4, Pages 249-256. <https://doi.org/10.1097/MAJ.0b013e31803b900f>
- [8] H. Louis, T. C. Egemonye, T. O. Unimuke."Detection of Carbon, Sulfur, and Nitrogen Dioxide Pollutants with a 2D Ca12O12 Nanostructured Material". *ACS Omega* 2022, 7, 34929–34943. <https://doi.org/10.1021/acsomega.2c03512> <https://doi.org/10.1111/ina.13170>
- [9] Z. Chen, N. Liu, H.Tang, X. Gao, Y. Zhang, H. Kan. "Health effects of exposure to sulfur dioxide, nitrogen dioxide, ozone, and carbon monoxide between 1980 and 2019: A systematic review and meta-analysis". *Indoor Air*. 2022 Nov;32(11). <https://doi.org/10.1111/ina.13170>
- [10] J. O. Anderson, J. G. Thundiyil, A. Stolbach."Clearing the Air: A Review of the Effects of Particulate Matter Air Pollution on Human Health". *J Med Toxicol*. 2012 Jun; 8(2): 166–175. <https://doi.org/10.1007/s13181-011-0203-1>
- [11] M. B. Marinov, I. Topalov, E. Gieva and G. Nikolov, "Air quality monitoring in urban environments," 2016 39th International Spring Seminar on Electronics Technology (ISSE), Pilsen, Czech Republic, 2016, pp. 443-448, <https://doi.org/10.1109/ISSE.2016.7563237>.
- [12] W.M. Shaban, X. Dongxi, K. S. Daef, K. Elbaz. "Real-time early warning and the prediction of air pollutants for sustainable development in smart cities". *Atmospheric Pollution Research*, Volume 15, Issue 7. <https://doi.org/10.1016/j.apr.2024.102162>.
- [13] S. C. Anenberg, M. Bindl, M. Brauer, J. J. Castillo, S. Cavalieri, B. N. Duncan. Using Satellites to Track Indicators of Global Air Pollution and Climate Change Impacts: Lessons Learned From a NASA-Supported Science-Stakeholder Collaborative. *Geohealth* Volume4, Issue 7, July 2020, e2020GH000270. <https://doi.org/10.1029/2020GH000270>
- [14] A. S. P. Arimurti, B. M. Sukojo. Monitoring of Air Quality Changes using Landsat 8-9 Data in 2018-2022. *IOP Conference Series: Earth and Environmental Science*, Volume 1276, Geomatics International Conference 2023. <https://doi.org/10.1088/1755-1315/1276/1/012036>
- [15] I. Saraswat, R. K. Mishra, A. Kumar. Estimation of PM10 concentration from Landsat 8 OLI satellite imagery over Delhi, India. *Remote Sensing Applications: Society and Environment* Volume 8, November 2017, Pages 251-257. <https://doi.org/10.1016/j.rsase.2017.10.006>

- [16] D. L. Setyowati, E. Handoyo, P. Hardati, M. Amin. "Potentials Of Green Open Spaces In Air Quality Control Of Semarang City, Indonesia". *Pollution Research* March 2022. <https://doi.org/10.53550/PR.2022.v4i101.010>
- [17] B. Pigawati, N. Yuliasuti, F. H. Mardiansjah. "The Settlements Growth in Mijen District, Suburb of Semarang". *IOP Conference Series: Earth and Environmental Science*, Volume 123, 123 012034. <https://doi.org/10.1088/1755-1315/123/1/012034>
- [18] G.G.Z. Viedra, B. M. Sukojo, B. M. "Analysis of The Effect of Deforestation Rates on Air Pollution Concentration and Land Surface Temperature Using Landsat-8 Imagery with Google Earth Engine (Case Study: East Kalimantan Province, 2019-2020)". *IOP Conference Series: Earth and Environmental Science*, 1127(1), 012032. <https://doi.org/10.1088/1755-1315/1127/1/012032>
- [19] A. M. Solihin, N. Putri. "Keragaman Penggunaan Lahan Eksisting di Hulu Sub DAS Cikapundung Berdasarkan Indeks Vegetasi dan Temperatur Permukaan Lahan". *Agrikultura*, 31(3), 255. <https://doi.org/10.24198/agrikultura.v31i3.29467>
- [20] A. Kumar, R. Ratnam, & A. P. Krishna. "Detection of Coal Mine Fire Using Landsat-8 OLI/TIRS Satellite Data in Ramgarh and Hazaribagh Coalfields, India". *Recent Technologies for Disaster Management and Risk Reduction* 451–464.. [https://doi.org/10.1007/978-3-030-76116-5\\_23](https://doi.org/10.1007/978-3-030-76116-5_23) . Springer.
- [21] M. Dede, M. A. Widiawaty, N. Nurhanifah, A. Ismail, A. R. P. Artati, A. Ati, Y. R. Ramadhan. Estimasi Perubahan Kualitas Udara Berbasis Citra Satelit Penginderaan Jauh Di Sekitar PLTU Cirebon. *Jambura Geoscience Review*, 2(2), 78–87. <https://doi.org/10.34312/jgeosrev.v2i2.5951>
- [22] N. Othman, M. Z. Mat Jafri, L. H. San. Estimating Particulate Matter Concentration over Arid Region Using Satellite Remote Sensing: A Case Study in Makkah, Saudi Arabia. *Modern Applied Science*, 4(11). <https://doi.org/10.5539/mas.v4n11p131>
- [23] F. A. Alseroury. "The Effect Of Pollutants On Land Surface Temperature Around Power Plant" . *International Journal of Mechanical And Production Engineering*, 3(11), 17–21.